crystals

MDPI

Article

Rayleigh Waves Propagating in the Functionally Graded One-Dimensional Hexagonal Quasicrystal Half-Space

Bo Zhang [1,2,3], Honghang Tu [1], Liangjuan Li [4], Jiangong Yu [1] and Jun Dai [1,*]

[1] School of Mechanical and Power Engineering, Henan Polytechnic University, Jiaozuo 454003, China; bozhanghpu@hpu.edu.cn (B.Z.); thh@home.hpu.edu.cn (H.T.); yuee@hpu.edu.cn (J.Y.)
[2] School of Safety Science and Engineering, Henan Polytechnic University, Jiaozuo 454003, China
[3] Guangdong Xinhuan Electromechanical Equipment Manufacturing Co., Ltd., Zhongshan 528429, China
[4] School of Mathematics and Information Science, Henan Polytechnic University, Jiaozuo 454003, China; llj@hpu.edu.cn
* Correspondence: daijun0922@hpu.edu.cn

Abstract: For the manufacturing and optimization of quasicrystal structures, Rayleigh waves propagating in the functionally graded one-dimensional hexagonal quasicrystal half-space are investigated. The analytical Laguerre orthogonal polynomial method is employed to solve dynamic equations of wave motion, which greatly improves the computational efficiency. Dispersion curves and displacement distributions are illustrated. The influences of the phonon–phason coupling effect, inhomogeneity, and quasiperiodic direction on wave characteristics are analyzed. Some new results are obtained: (1) Compared with the classical Laguerre polynomial method, the improvement in computational efficiency of the analytical Laguerre polynomial method is more than 99%. (2) The energy penetration depth of phason modes is greater than that of phonon modes. The results lay a theoretical foundation for designing and optimizing SAW devices.

Keywords: quasicrystal; Rayleigh waves; functionally graded material; phonon–phason coupling effect; Laguerre orthogonal polynomials method

check for updates

Citation: Zhang, B.; Tu, H.; Li, L.; Yu, J.; Dai, J. Rayleigh Waves Propagating in the Functionally Graded One-Dimensional Hexagonal Quasicrystal Half-Space. *Crystals* **2023**, *13*, 1205. https://doi.org/10.3390/cryst13081205

Academic Editor: Alessandro Chiasera

Received: 18 July 2023
Revised: 30 July 2023
Accepted: 31 July 2023
Published: 3 August 2023

Copyright: © 2023 by the authors. Licensee MDPI, Basel, Switzerland. This article is an open access article distributed under the terms and conditions of the Creative Commons Attribution (CC BY) license (https://creativecommons.org/licenses/by/4.0/).

1. Introduction

As a novel kind of solid matter, the quasicrystal (QC) was first discovered from a diffraction image of rapidly cooled Al-Mn alloys by Shechtman et al. [1] in 1982. The discovery is revolutionary because QCs have a long-range quasiperiodic translational order and a long-range orientational order. Natural quasicrystals were discovered in volcanic ash in 2009. Due to their nonperiodic atomic structure, QCs possess a series of superior properties, such as low adhesion, low coefficient of friction, low porosity, low thermal conductivity, high abrasion resistance, and high resistivity [2–6]. They are predominantly used as coatings or thin films of metals in the automotive, aerospace, and energy industries.

Multilayered structures are commonly used in engineering. They can take advantage of the excellcent performances of each layer. However, multilayered structures face several limitations at their interfaces. These limitations include issues like delamination and cracking, stress concentration, and abrupt stress changes. To overcome these limitations, the best way is to eliminate interfaces. To this end, functionally graded material (FGM) was first proposed by Japanese scientists, whose properties vary in a continuous gradient in one direction [7,8]. Subsequently, they are used in mechanical engineering, aerospace engineering, and so on. In recent years, several methods have been developed by researchers to investigate the mechanical behaviors of FGM structures. These methods are mainly divided into three kinds: numerical simulation, matrix, and analytical methods. The numerical methods include the finite element method [9], the boundary element method [10], and the semi-analytical finite element method [11]. They not only have a high computational accuracy but can also be adapted to various complex shapes. However, they need more

time to obtain solutions. The matrix methods include the stiffness matrix method [12], the reverberation-ray matrix method [13], the dual-variable and position method [14], and so on. The dual-variable and position method is an appealing technique that remains stable even when dealing with large or small λ values and thin or thick layers [15]. Therefore, it perfectly overcomes the drawbacks of other matrix methods. However, when dealing with FGM structures, they are usually divided into N layers to approximate the continuous variation in material properties. The bigger the N, the more accurate the results, but the longer the calculation time needed. The analytical methods, such as the power series method [16] and the orthogonal polynomial method [17], can obtain approximate analytical expressions. So, their computational efficiency is high. When dealing with FGM structures, by assuming the parameters to be functions of variables in the thickness direction, these two methods do not require delamination.

With the development of material preparation technology, functionally graded quasicrystal (FGQC) materials have been prepared [18,19]. Meanwhile, mechanical investigations on FGQC structures have been conducted to promote their applications. The mechanical behaviors of two-dimensional functionally graded piezoelectric quasicrystal (FGPQC) wedges and spaces subjected to line force, charge, or dislocation were investigated by Mu et al. [20]. In the context of nonlocal strain gradient theory, the bending behavior of one-dimensional hexagonal FGPQC multilayered nanoplates was studied by Zhang et al. [21]. By utilizing the integral transform technique, Yang et al. [22] investigated the interaction between SH waves and a crack in one-dimensional hexagonal FGPQC structures. Axisymmetric bending analysis of a one-dimensional hexagonal FGPQC circular plate was performed by Li et al. [23]. By using the Legendre polynomial method, Zhang et al. studied guided waves propagating in FGQC plates [24] and cylinders [25].

From the above simple review, although the mechanical behaviors of FGQC structures have received a lot of attention, no references to Rayleigh waves in the FGQC half-space are available. Rayleigh waves were first investigated by Rayleigh in 1885 [26]. In these waves, the particle motion amplitude decreases with an exponential decay along with depth, so the energy is mainly concentrated on the surface. Accordingly, they have been widely used for defect detection near surfaces [27] and the design and optimization of SAW devices [28]. Also to this end, Rayleigh waves propagating in the FGQC half-space were investigated by using the analytical Laguerre orthogonal polynomial method in the present study.

The Laguerre orthogonal polynomial method (LOPM) was proposed by Maradudin et al. [29] to investigate acoustic waves in homogeneous semi-infinite wedges. It has the following features: (1) by assuming position-dependent material constants, the boundary conditions are incorporated directly into equations of motion; (2) each independent variable is expanded in a Laguerre orthonormal polynomial series, then the motion equations are converted into a matrix eigenvalue problem; (3) it does not need delamination when dealing with FGM structures. In recent years, this method has been employed to investigate surface waves and vibrations [30–32]. However, there are a lot of numerical integrations in the solving process of the traditional polynomial method [33], which wastes a lot of time. If the analytical expressions of these integrations are deduced, the computational efficiency would be improved greatly, which is similar to the analytical Legendre polynomial method [34]. Accordingly, the analytical expressions of the dynamic equations of Rayleigh waves in FGQC half-space are deduced in this paper. Dispersion curves and displacement distributions are illustrated. The influences of the phonon–phason coupling effect, inhomogeneity, and quasiperiodic direction on wave characteristics are analyzed.

2. Mathematics and Formulation

A one-dimensional hexagonal FGQC half-space in the Cartesian coordinate system is shown in Figure 1. Material properties vary gradually in the z direction. Rayleigh waves propagate in the x direction. The traction-free condition at the top surface is assumed.

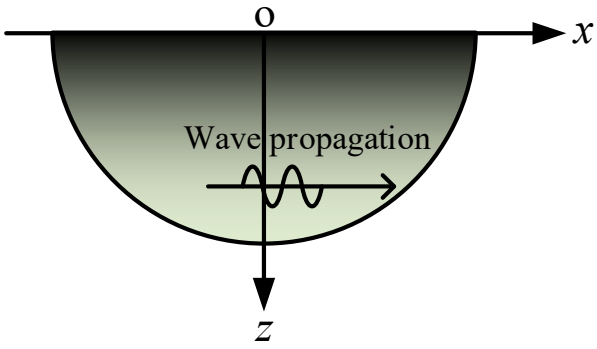

Figure 1. Schematic diagram of a one-dimensional hexagonal FGQC half-space.

Based on the Bak model [35], dynamic equations in the absence of body forces are written as follows:

$$T_{ij,j} = \rho \ddot{u}_i, H_{ij,j} = \rho \ddot{w}_i, \tag{1}$$

where T_{ij} and H_{ij} are phonon and phason stresses, respectively; u_i and w_i represent displacements in the phonon and phason fields, respectively; ρ is the density.

The strain–displacement relationship in the context of linear elasticity theory can be written as [36]:

$$\varepsilon_{ij} = \frac{1}{2}(u_{i,j} + u_{j,i}), w_{ij} = w_{i,j}, \tag{2}$$

where ε_{ij} and w_{ij}, respectively, represent phonon and phason strain.

As abovementioned, material properties vary gradually in the z direction. Material parameters can be expressed as functions of variable z. Meanwhile, by assuming position-dependent physical constants, the assumed boundary conditions can be automatically incorporated into the equations of motion [37]. It is an outstanding specificity of the orthogonal polynomial method. Therefore, material parameters are denoted in the following form:

$$\begin{array}{c} C_{ij}(z) = C_{ij} \times f_1(z) \times H(z), R_i(z) = R_i \times f_2(z) \times H(z), \\ K_i(z) = K_i \times f_3(z) \times H(z), \rho(z) = \rho \times f_4(z) \times H(z) \end{array} \tag{3}$$

where $f_i(z)(i = 1, 2, 3, 4)$ are the graded functions. They may be the same or different. C_{ij} and K_i are elastic parameters in the phonon and phason fields, respectively. R_i is the phonon–phason coupling coefficient.

The Heaviside unit step function $H(z)$ is introduced in Equation (3), which is denoted as follows:

$$H(z) = \begin{cases} 0, z < 0 \\ 1, z \geq 0 \end{cases} \tag{4}$$

$H(z)$ describes the region occupied by a material body.

$$\nabla H(z) = -\mathbf{n}\delta_s, \tag{5}$$

where δ_s is the Dirac delta function.

For the one-dimensional quasicrystal half-space, its internal atomic arrangement is quasiperiodic just in one direction. The quasiperiodic direction may be in the x, y, or z direction. If the quasiperiodic direction is along the x direction, the atomic arrangement in the y and z directions is periodic, and the half-space is defined as the x-FGQC half-space. Similarly, if the quasiperiodic direction is along the y direction, the atomic arrangement in the x and z directions is periodic, and the half-space is defined as the y-FGQC half-space. If the quasiperiodic direction is along the z direction, the atomic arrangement in the x and y directions is periodic, and the half-space is defined as the z-FGQC half-space. In this paper, Rayleigh waves propagating in the x- and z-FGQC half-spaces are investigated. The

reason is that the phonon–phason coupling effect has an influence on SH waves in *y*-FGQC half-spaces, which is similar to *y*-FGQC plates [24].

(1) *z*-FGQC half-space

For the *z*-FGQC half-space, only the phason displacement component, w_z, in the z direction is not 0. So, its displacements can be written in the following form:

$$u_x(x,z,t) = U(z)e^{i(kx-\omega t)}, u_z(x,z,t) = W(z)e^{i(kx-\omega t)}, w_z(x,z,t) = \gamma(z)e^{i(kx-\omega t)}, \quad (6)$$

where $U(z)$ and $W(z)$ are the amplitudes of the phonon displacement components in the x and z directions, respectively; $\gamma(z)$ is the phason displacement component in the z direction; k is the wavenumber; and ω is the angular frequency.

According to the generalized Hooke's law, the constitutive equations for 1D hexagonal QCs are written as follows [38]:

$$\begin{array}{l} T_{xx} = C_{11}(z)\varepsilon_{xx} + C_{12}(z)\varepsilon_{yy} + C_{13}(z)\varepsilon_{zz} + R_1(z)w_{zz} \\ T_{yy} = C_{12}(z)\varepsilon_{xx} + C_{22}(z)\varepsilon_{yy} + C_{13}(z)\varepsilon_{zz} + R_1(z)w_{zz} \\ T_{zz} = C_{13}(z)\varepsilon_{xx} + C_{13}(z)\varepsilon_{yy} + C_{33}(z)\varepsilon_{zz} + R_2(z)w_{zz} \\ T_{zy} = 2C_{55}(z)\varepsilon_{zy} + R_3(z)w_{zy} \\ T_{xz} = 2C_{55}(z)\varepsilon_{zx} + R_3(z)w_{zx} \\ T_{xy} = 2C_{66}(z)\varepsilon_{xy} \\ H_{zz} = R_1(z)\varepsilon_{xx} + R_1(z)\varepsilon_{yy} + R_2(z)\varepsilon_{zz} + K_1(z)w_{zz} \\ H_{zx} = 2R_3(z)\varepsilon_{zx} + K_2(z)w_{zx} \\ H_{zy} = 2R_3(z)\varepsilon_{yz} + K_2(z)w_{zy} \end{array}, \quad (7)$$

where T_{ij} and H_{ij} ($i, j = x, y$, and z) are phonon and phason stress components, respectively.

By substituting Equations (2)–(7) into Equation (1), the following differential governing equations of wave motion are deduced:

$$\begin{array}{l} [-k^2C_{11}(z)U + C_{55}(z)U'' + ik(C_{13}(z) + C_{55}(z))W' + ik(R_1(z) + R_3(z))\gamma' + ikC_{55}{}'(z)W \\ +C_{55}{}'(z)U' + ikR_3{}'(z)\gamma]H(z) + (ikC_{55}(z)W + C_{55}(z)U' + ikR_3(z)\gamma)H'(z) = -\rho(z)\omega^2U \end{array} \quad (8)$$

$$\begin{array}{l} [-k^2C_{55}(z)W + C_{33}(z)W'' + ik(C_{13}(z) + C_{55}(z))U' - k^2R_3(z)\gamma + R_2(z)\gamma'' + ikC_{13}{}'(z)U \\ +C_{33}{}'(z)W' + R_2{}'(z)\gamma']H(z) + (ikC_{13}(z)U + C_{33}(z)W' + R2(z)\gamma')H'(z) = -\rho(z)\omega^2W \end{array} \quad (9)$$

$$\begin{array}{l} [-k^2R_3(z)W + R_2(z)W'' + ik(R_1(z) + R_3(z))U' - k^2K_2(z)\gamma + K_1(z)\gamma'' + ikR_1{}'(z)U \\ +R_2{}'(z)W' + K_1{}'(z)\gamma']H(z) + (ikR_1(z)U + R_2(z)W' + K_1(z)\gamma')H'(z) = -\rho(z)\omega^2\gamma \end{array} \quad (10)$$

where the superscript (′) indicates the derivation of z.

As can be seen from Equations (8)–(10), the assumed traction-free condition is incorporated directly into the equations of motion. For Rayleigh waves propagating in *z*-FGQC half-spaces, the assumed traction-free condition requires stress components in the z direction be 0 at the top surface ($T_{zz} = T_{xz} = H_{zz} = 0$ at $z = 0$). This way of dealing with the boundary condition has been used by several researchers [29–34]. To see how to ensure the assumed traction-free condition at the top surface, based on the divergence theorem, the theoretical validation was detailed by Lefebvre et al. [37] to show how position-dependent physical constants can fulfill this role. Specifically, this method can also be used to deal with other boundary conditions; see the available references [37,39].

Subsequently, $U(z)$, $W(z)$, and $\gamma(z)$ are written as the Laguerre polynomial series.

$$U(z) = \sum_{m=0}^{\infty} p_m^1 L_m(z), W(z) = \sum_{m=0}^{\infty} p_m^2 L_m(z), \gamma(z) = \sum_{m=0}^{\infty} r_m^1 L_m(z), \quad (11)$$

where $p_m^i (i = 1, 2)$ and r_m^1 are coefficients of polynomial expansions to be solved. $L_m(z) = e^{(-\frac{1}{2}z)} \cdot P_m(z)$ with $P_m(z)$ being the m-order Laguerre polynomial; m runs theoretically from 0 to ∞. Equation (11) becomes convergent as m runs to a finite value M. The value of M is determined according to the actual need of calculation. For the Rayleigh

waves in the present paper, the larger the value of M, the more convergent modes there are, but the longer the calculation time.

Multiply Equations (8)–(10) by $L_j(z)$ with j running from 0 to M. Then, integrating over z from 0 to ∞, the following equation can be obtained:

$$\begin{cases} A_{11}^{j,m} p_m^1 + A_{12}^{j,m} p_m^2 + A_{13}^{j,m} r_m^1 = -\omega^2 M_m^j p_m^1 \\ A_{21}^{j,m} p_m^1 + A_{22}^{j,m} p_m^2 + A_{23}^{j,m} r_m^1 = -\omega^2 M_m^j p_m^2 \\ A_{31}^{j,m} p_m^1 + A_{32}^{j,m} p_m^2 + A_{33}^{j,m} r_m^1 = -\omega^2 M_m^j r_m^1 \end{cases} \tag{12}$$

where $A_{\alpha\beta}^{j,m}(\alpha, \beta = 1, 2, 3)$ and M_m^j can be obtained according to Equation (8–10), which are detailed as follows:

$$\begin{array}{l} A_{11}^{j,m} = -k^2 \times C_{11} \times u_1[m,0,j,0] + C_{55} \times u_1[m,0,j,2] + C_{55} \times F_1[m,0,j,1] \\ A_{12}^{j,m} = I \times k \times C_{13} \times u_1[m,0,j,1] + I \times k \times C_{55} \times u_1[m,0,j,1] + I \times k \times C_{55} \times F_1[m,0,j,0] \\ A_{13}^{j,m} = I \times k \times (R_1 + R_3) \times u_2[m,0,j,1] + I \times k \times R_3 \times F_2[m,0,j,0] \\ A_{21}^{j,m} = I \times k \times C_{13} \times u_1[m,0,j,1] + I \times k \times C_{55} \times u_1[m,0,j,1] + I \times k \times C_{13} \times F_1[m,0,j,0] \\ A_{22}^{j,m} = -k^2 \times C_{55} \times u_1[m,0,j,0] + C_{33} \times u_1[m,0,j,2] + C_{33} \times F_1[m,0,j,1] \\ A_{23}^{j,m} = -k^2 \times R_3 \times u_2[m,0,j,0] + R_2 \times u_2[m,0,j,2] + R_2 \times F_2[m,0,j,1] \\ A_{31}^{j,m} = I \times k \times (R_1 + R_3) \times u_2[m,0,j,1] + I \times k \times R_1 \times F_2[m,0,j,0] \\ A_{32}^{j,m} = -k^2 \times R_3 \times u_2[m,0,j,0] + R_2 \times u_2[m,0,j,2] + R_2 \times F_2[m,0,j,1] \\ A_{33}^{j,m} = -k^2 \times K_2 \times u_3[m,0,j,0] + K_1 \times u_3[m,0,j,2] + K_1 \times F_3[m,0,j,1] \\ M_j^m = \rho \times u_4[m,0,l,0] \end{array} \tag{13}$$

where

$$\begin{aligned} u_i[m,h,j,l] = \quad & (1+A_i) \times \int_0^\infty H(z) z^h L_j(z) \tfrac{\partial^l L_m(z)}{\partial z^l} dz - A_i \times \int_0^\infty H(z) z^h L_j(z) \tfrac{\partial^l L_m(z)}{\partial z^l} e^{-\alpha z} dz \\ F_i[m,h,j,l] = \quad & (1+A_i) \times \int_0^\infty \tfrac{dH(z)}{dz} z^h L_j(z) \tfrac{\partial^l L_m(z)}{\partial z^l} dz - A_i \times \int_0^\infty \tfrac{dH(z)}{dz} z^h L_j(z) \tfrac{\partial^l L_m(z)}{\partial z^l} e^{-\alpha z} dz \\ & + \alpha \times A_i \times \int_0^\infty H(z) z^h L_j(z) \tfrac{\partial^l L_m(z)}{\partial z^l} e^{-\alpha z} dz \end{aligned}$$

Equation (12) is transformed into a matrix system.

$$\begin{bmatrix} A_{11}^{j,m} & A_{12}^{j,m} & A_{13}^{j,m} \\ A_{21}^{j,m} & A_{22}^{j,m} & A_{23}^{j,m} \\ A_{31}^{j,m} & A_{32}^{j,m} & A_{33}^{j,m} \end{bmatrix} \begin{Bmatrix} p_m^1 \\ p_m^2 \\ r_m^1 \end{Bmatrix} = -\omega^2 \begin{bmatrix} M_m^j & 0 & 0 \\ 0 & M_m^j & 0 \\ 0 & 0 & M_m^j \end{bmatrix} \begin{Bmatrix} p_m^1 \\ p_m^2 \\ r_m^1 \end{Bmatrix}, \tag{14}$$

At this point, it is transformed into a matrix eigenvalue problem. Computer programs were written to solve the eigenvalues and eigenvectors. For a given k, the phase velocity is obtained by $V_{ph} = \sqrt{eigenvalue[k]}/k$. By substituting eigenvectors into Equation (9), displacements are calculated.

(2) x-FGQC half-space

The atomic arrangement is quasiperiodic only in the x direction in the x-FGQC half-space. The phason displacement component in the x direction is $w_x(x,z,t) = \beta(z)e^{ikx - i\omega t}$; the phason displacement components in other two directions are 0, i.e., $w_y(x,z,t) = w_z(x,z,t) = 0$. The phonon displacements are the same as in Equation (4).

According to the generalized Hooke's law, the constitutive equations for the 1D hexagonal x-FGQC are written as follows:

$$\begin{array}{l} T_{yy} = C_{11}(z)\varepsilon_{yy} + C_{12}(z)\varepsilon_{zz} + C_{13}(z)\varepsilon_{xx} + R_1(z)w_{xx} \\ T_{zz} = C_{12}(z)\varepsilon_{yy} + C_{22}(z)\varepsilon_{zz} + C_{13}(z)\varepsilon_{xx} + R_1(z)w_{xx} \\ T_{xx} = C_{13}(z)\varepsilon_{yy} + C_{13}(z)\varepsilon_{zz} + C_{33}(z)\varepsilon_{xx} + R_2(z)w_{xx} \\ T_{yz} = 2C_{66}(z)\varepsilon_{yz} \\ T_{xz} = 2C_{44}(z)\varepsilon_{xz} + R_3(z)w_{xz} \\ T_{xy} = 2C_{44}(z)\varepsilon_{xy} + R_3(z)w_{xy} \\ H_{xx} = R_2(z)\varepsilon_{xx} + R_1(z)\varepsilon_{yy} + R_1(z)\varepsilon_{zz} + K_1(z)w_{xx} \\ H_{xz} = 2R_3(z)\varepsilon_{xz} + K_2(z)w_{xz} \\ H_{xy} = 2R_3(z)\varepsilon_{xy} + K_2(z)w_{xy} \end{array} . \quad (15)$$

By substituting Equations (2) and (15) into Equation (1), the following differential governing equations are deduced:

$$\begin{array}{c} [-k^2C_{33}(z)U + C_{44}(z)U'' + ik(C_{13}(z) + C_{55}(z))W' - k^2R_2(z)\beta + R_2(z)\beta'' + ikC_{44}{}'(z)W \\ +C_{44}{}'(z)U' + R_3{}'(z)\beta']H(z) + (ikC_{44}(z)W + C_{44}(z)U' + R_3(z)\beta')H'(z) = -\rho(z)\omega^2U \end{array} \quad (16)$$

$$\begin{array}{c} [-k^2C_{44}(z)W + C_{22}(z)W' + ik(C_{13}(z) + C_{44}(z))U' + ik(R_1(z) + R_3(z))\beta' + ikC_{13}{}'(z)U \\ +C_{22}{}'(z)W' + ikR_1{}'(z)\beta]H(z) + (ikC_{13}(z)U + C_{22}(z)W' + ikR_1(z)\beta)H'(z) = -\rho(z)\omega^2W \end{array} \quad (17)$$

$$\begin{array}{c} [-k^2R_2(z)U + R_3(z)U'' + ik(R_1(z) + R_3(z))W' - k^2K_1(z)\beta + K_2(z)\beta'' + ikR_3{}'(z)W \\ +R_2{}'(z)U' + K_1{}'(z)\beta']H(z) + (ikR_1(z)W + R_2(z)U' + K_1(z)\beta')H'(z) = -\rho(z)\omega^2\beta \end{array} \quad (18)$$

As can be seen from Equations (16)–(18), the assumed traction-free condition is incorporated directly into the equations of motion. For *x*-FGQC half-spaces, the assumed traction-free condition means that the stress components in the z direction are 0 at the top surface ($T_{zz} = T_{xz} = H_{xz} = 0$ at $z = 0$).

Subsequently, $U(z)$, $W(z)$, and $\beta(z)$ are written as a Laguerre polynomial series.

$$U(z) = \sum_{m=0}^{\infty} p_m^1 L_m(z), W(z) = \sum_{m=0}^{\infty} p_m^2 L_m(z), \beta(z) = \sum_{m=0}^{\infty} r_m^2 L_m(z), \quad (19)$$

The detailed solving process is the same as that of the *z*-FGQC half-space; it is not given here.

3. Analytical Integration Expression of Laguerre Polynomial Method

To solve Equation (13), a lot of numerical integrations are required when using the traditional Laguerre polynomial method, which would be very time consuming. We replaced the numerical integrations with analytical integrations in the Legendre polynomial method. It has been used to investigate guided waves in plates and hollow cylinders [34,40]. The results demonstrated that the calculation efficiency was hugely improved. Motivated by it, we had the idea that if the analytical expressions of these integrations in Equation (13) are deduced, the computational efficiency would be improved greatly. When the gradient function is an exponential function, there are some products of the exponential function and Laguerre orthogonal polynomials. Their integration can be calculated in the form of summation. Thus, the computational speed would improve greatly.

From the above Equation (13), all integrations can be summarized as the following 10 equations:

$$\begin{array}{ll} I_1 = \int_0^\infty L_m(z)L_j(z)dz & I_2 = \int_0^\infty \frac{dL_m(z)}{dz}L_j(z)dz \\ I_3 = \int_0^\infty \frac{d^2L_m(z)}{dz^2}L_j(z)dz & I_4 = \int_0^\infty L_m(z)L_j(z)e^{-\alpha z}dz \\ I_5 = \int_0^\infty \frac{dL_m(z)}{dz}L_j(z)e^{-\alpha z}dz & I_6 = \int_0^\infty \frac{d^2L_m(z)}{dz^2}L_j(z)e^{-\alpha z}dz \\ I_7 = \int_0^\infty L_m(z)L_j(z)\delta(z)dz & I_8 = \int_0^\infty L_m(z)L_j(z)\delta(z)e^{-\alpha z}dz \\ I_9 = \int_0^\infty \frac{dL_m(z)}{dz}L_j(z)\delta(z)e^{-\alpha z}dz & I_{10} = \int_0^\infty \frac{d^2L_m(z)}{dz^2}L_j(z)\delta(z)e^{-\alpha z}dz \end{array} , \quad (20)$$

where $\delta(z) = \frac{dH(z)}{dz}$.

In combination with Newton's generalized binomial theorem and the Cauchy product, these integrations can be easily transformed into the form of summation by utilizing the generating function method [41]. According to the properties of Laguerre polynomials, the generating function used in this paper is as follows:

$$\frac{1}{1-s}e^{-\frac{1}{2}z\left(\frac{1+s}{1-s}\right)} = \sum_{m=0}^{\infty} s^m L_m(z). \tag{21}$$

The first few of these functions are:

$$\begin{array}{l} L_0(z) = e^{-z/2}, \\ L_1(z) = e^{-z/2}(1-z), \\ L_2(z) = e^{-z/2}\left(1-2z+\frac{1}{2}z^2\right), \\ L_3(z) = e^{-z/2}\left(1-3z+\frac{3}{2}z^2-\frac{1}{6}z^3\right), \\ \cdots \end{array} \tag{22}$$

The recurrence formula satisfied by $L_m(z)$ is as follows:

$$L_{m+1}(z) = \frac{2m+1-z}{m+1}L_m(z) - \frac{m}{m+1}L_{m-1}(z). \tag{23}$$

With the help of Equations (21)–(23), the analytical expressions of Equation (20) can be deduced for the first time, as follows:

$$\begin{array}{ll} I_1 = \delta_{jm} & I_2 = -\frac{1}{2}\delta_{jm} - \Omega(m-j-1) \\ I_3 = \frac{1}{4}\delta_{jm} + (m-j)\Omega(m-j-1) & I_4 = T_{jm} \\ I_5 = -\frac{1}{2}T_{jm} - \sum_{p=0}^{m-1} T_{jp} & I_6 = \frac{1}{4}T_{jm} - (m-p)\sum_{p=0}^{m-1} T_{jp} \\ I_7 = I_8 = 1 & I_9 = I_{10} = -\frac{1}{2} - m \end{array}, \tag{24}$$

where

$$\delta_{jm} = \begin{cases} 1 & j = m \\ 0 & j \neq m \end{cases}$$

$$\Omega(m-j-1) = \begin{cases} 1 & m-j-1 \quad \text{is non-negative integer} \\ 0 & \text{else} \end{cases}$$

$$T_{jm} = \sum_{p=0}^{\min[j,m]} \frac{(j+m-p)!(1-\alpha)^p \alpha^{m+j-2p}}{(m-p)!p!(j-p)!(1+\alpha)^{m+j+1-p}}$$

By substituting Equation (24) into Equation (13), the analytical expressions of Equation (13) can be deduced. For example:

$$\begin{array}{l} u_1[m,0,j,0] = (1+A_1) \times \int_0^{\infty} H(z)L_j(z)L_m(z)dz - A_1 \times \int_0^{\infty} H(z)L_j(z)L_m(z)e^{-\alpha z}dz \\ = (1+A_1) \times I_1 - A_1 \times I_4 = (1+A_1) \times \delta_{jm} - A_1 \times T_{jm} \end{array}$$

4. Numerical Results

Based on the above equations in Sections 2 and 3, computer programs were written by using software "Wolfram Mathematica" of Wolfram Research, Inc. (Champaign, IL, USA) to calculate eigenvalues and eigenvectors. Subsequently, dispersion, displacement, and stress distributions were obtained by substituting them into the corresponding equations.

The FGQC half-spaces are composed of two kinds of quasicrystal materials, named QC1 and QC2. Their material coefficients are listed in Table 1 [24]. The material density and hardness of QC1 are small, and its thermal stability is low, whereas the material density and hardness of QC2 are large, and its thermal stability is high. Therefore, combining these materials allows the desired material density, hardness, and thermal stability to be obtained.

Table 1. Coefficients of QC1 and QC2 [24].

	C_{11}	C_{12}	C_{13}	C_{22}	C_{23}	C_{33}	C_{44}	C_{55}
QC1	23.433	5.741	6.663	23.433	6.663	23.222	7.019	7.019
QC2	20	10	10	20	10	15	5	5
	C_{66}	ρ	R_1	R_2	R_3	K_1	K_2	
QC1	8.846	4.186	8.846	8.846	0.8846	12.2	2.4	
QC2	5	5.07	0.5	0.5	0.5	5	2	

Units: C_{ij} (10^{10} N/m^2), ρ (10^3 kg/m^3), R_i (10^8 N/m^2), and K_i (10^{10} N/m^2).

To calculate equivalent coefficients, the following exponential gradient function was chosen [42].

$$f(z) = f_\infty + (f_0 - f_\infty)e^{-\alpha z}, \tag{25}$$

where α is the coefficient of the graded function. f_0 and f_∞ are material coefficients at $z = 0$ and $z \to \infty$, respectively.

A relative coefficient of variation is introduced.

$$A = (f_\infty - f_0)/f_0 \tag{26}$$

Thus, Equation (25) is transformed as:

$$f_i(z) = f_0(1 + A_i - A_i e^{-\alpha z}) \tag{27}$$

In this study, three coefficients of graded function were taken into account, i.e., α = 1.5, 3, and 5.

4.1. Method Validation

To the best of our knowledge, few references on Rayleigh waves in FGQC half-spaces are available. To validate the present method, $A_i = R_i = K_i = 0$ was assumed to perform comparisons with the results from the crystal half-space. The material constants of aluminum (Al) are listed in Table 2. The corresponding displacement distributions are illustrated in Figure 2. The dotted lines are the results from reference [43], and the solid lines are results from the proposed method. It can be seen that these results from two different methods are the same; that is, the method presented in this paper can be used to solve Rayleigh wave characteristics.

Table 2. Material constants of aluminum.

C_{11}	C_{12}	C_{44}	ρ	E	σ
10.77	5.55	2.61	2.7	7	0.34

Units: C_{ij}, E (10^{10} N/m^2) and ρ (10^3 kg/m^3).

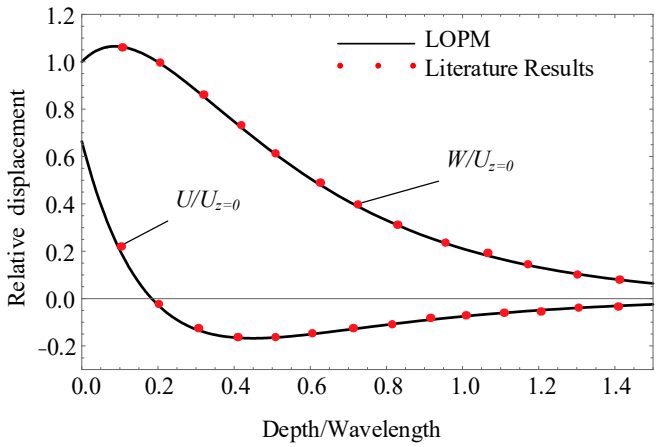

Figure 2. Relative displacement curves of the Al half-space.

4.2. Convergence and Computational Efficiency Analysis

Firstly, the convergence of the present method was investigated. It is universally known that the LOPM is an asymptotic method. Its convergence is determined by the finite value M. When M varies, Table 3 shows the phase velocities of the first phonon and phason modes for different k. It can be seen that the results are convergent when M = 16. Moreover, convergent speeds at high frequencies are slower than those at low frequencies.

Table 3. Phase velocity of the first phonon and phason modes with different k (km/s).

Mode	k	M = 2	M = 4	M = 8	M = 16	M = 32
The first phonon mode	0.5	2.922	2.913	2.912	2.912	2.912
	1	3.010	2.993	2.989	2.989	2.989
	2	3.183	3.139	3.122	3.121	3.121
The first phason mode	0.5	2.482	2.114	2.006	2.005	2.005
	1	2.175	2.037	1.996	1.994	1.994
	2	2.088	2.008	1.990	1.988	1.988

Subsequently, the computational efficiency of the present method was analyzed. The computer configuration used was as follows: CPU: Intel (Santa Clara, CA, USA) Core i7-9750 H, 2.6 GHz; RAM: 16 G. When α = 1.5, the calculation times of the classical Laguerre polynomial method (CLPA) and analytical Laguerre polynomial method (ALPA) are as listed in Table 4. Compared with the CLPA, the calculation time is significantly reduced. For example, when M = 10, the calculation time of the CLPA is 376.578 s, and that of ALPA is 0.812 s. The improvement in computational efficiency is more than 99%.

Table 4. When α = 1.5, integral calculation time t (s).

Method	M = 8	M = 9	M = 10	M = 11
CLPA	217.391	258.969	376.578	448.281
ALPA	0.360	0.469	0.812	0.875
Save	99.83%	99.82%	99.78%	99.80%

4.3. Phonon–Phason Coupling Effect

In this subsection, the phonon–phason coupling effect on the phase velocity and displacement distributions is described. Firstly, its influence on dispersion curves was investigated. When α = 1.5, Figure 3 shows the phase velocity dispersion curves of z-FGQC and the corresponding FGC half-space ($R_i = K_i = 0$; other material constants remained unchanged). Similar to the Lamb waves in FGQC plates, there are also two types of modes: phonon and phason modes, because the phonon field is responsible for particle motion, which is similar to the role of elastic fields in crystal structures. The dispersion curves consistent with elastic modes are named phonon modes. The other curves are named phason modes. It can be seen that the phonon modes and elastic modes in crystal half-spaces are almost the same. The reason for this is that the phonon–phason coupling effect on phonon modes is extremely weak, because R_i is much smaller than C_{ij} and K_i, as shown in Table 1.

Then, Figure 4 shows the phase velocity dispersion curves of z-FGQC half-space for different phonon–phason coupling coefficients. For a clearer observation, partially enlarged figures from Figure 4 are illustrated in Figure 5. As the phonon–phason coupling coefficient R_i increases, the phase velocity of the phonon modes increases and that of the phason modes decreases.

Subsequently, the phonon–phason coupling effect on the displacement distributions was investigated. When α = 1.5 and k = 1, Figures 6 and 7 illustrate the displacement distributions of the first phonon and phason modes, respectively. It can be seen that energies of the phonon and phason modes are mainly concentrated on the surface. Here,

the energies' propagating distance in the z direction is defined as the penetration depth, i.e., the depth where displacements decrease to zero. As can be seen, the penetration depth of the phason modes is greater than that of the phonon modes. Therefore, if the phason modes are used, defects at much deeper positions are detected. This feature is different from that of Lamb waves in FGQC plates [24]. Additionally, energies of phonon modes are mainly concentrated on the phonon displacement components, and the energies of the phason modes are mainly concentrated on the phason displacement components.

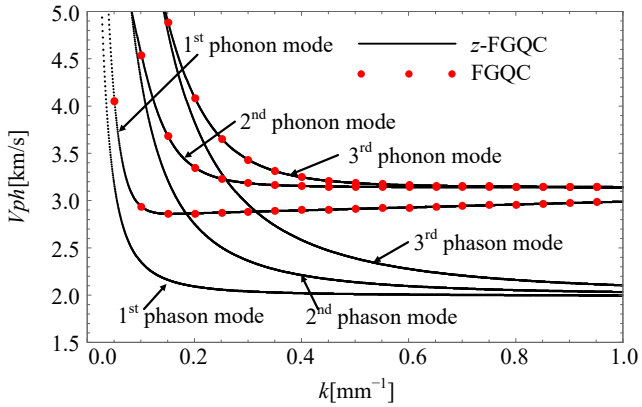

Figure 3. Phase velocity dispersion curves of z-FGQC and FGC half-spaces when $\alpha = 1.5$.

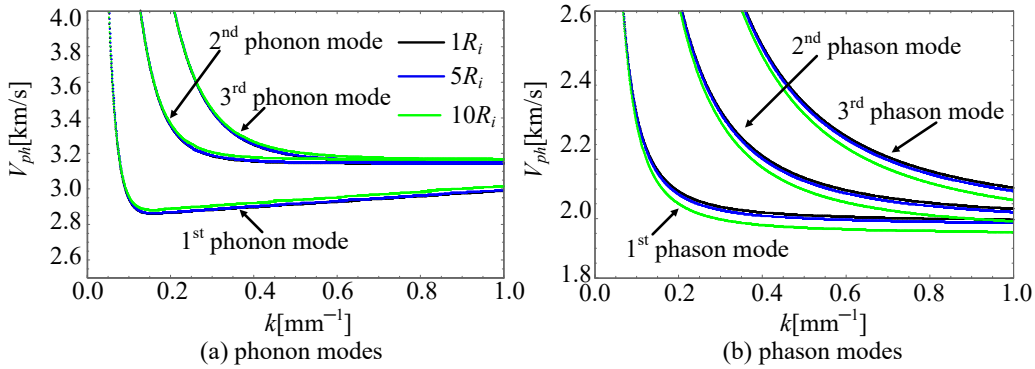

Figure 4. When $\alpha = 1.5$, phase velocity dispersion curves of z-FGQC half-spaces for different R_i.

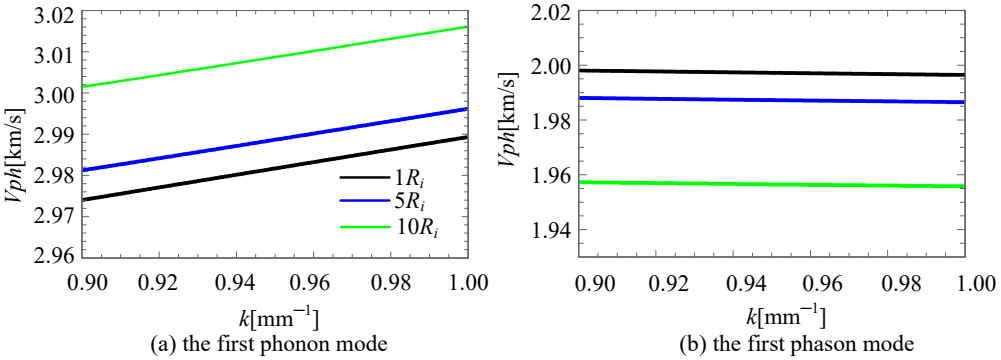

Figure 5. Partially enlarged figures from Figure 4.

As R_i increases, the phason displacement component of the phonon mode increases. But, the phonon displacement components have extremely weak variations. Different from phonon modes, as R_i increases, the phonon displacement components of the phason mode increase, and the phason displacement components have a weak variation.

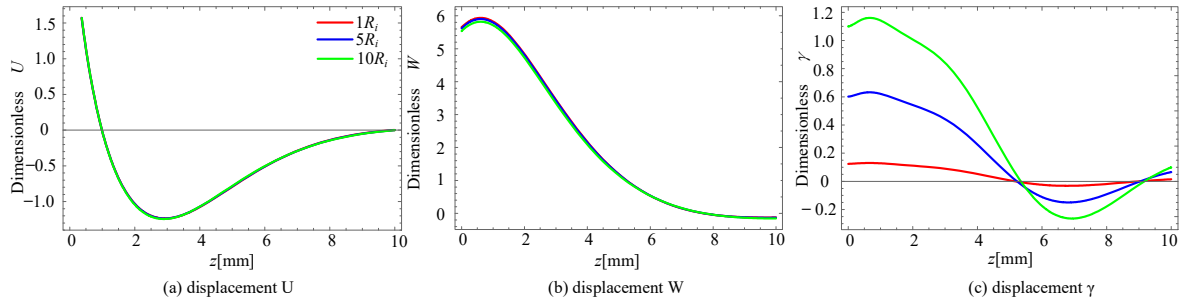

Figure 6. Displacement distributions of the first phonon mode when $\alpha = 1.5$ and $k = 1$.

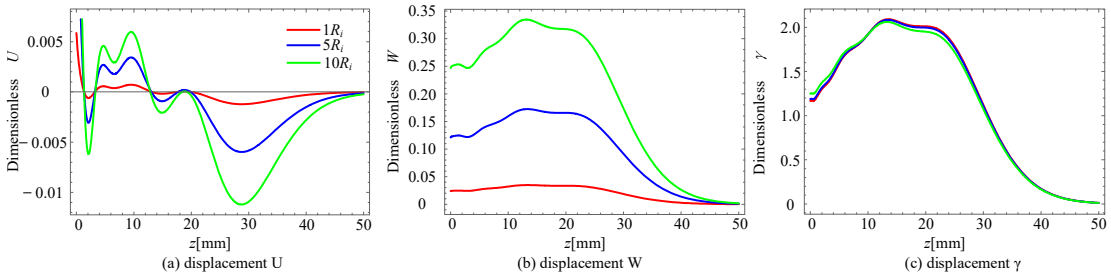

Figure 7. Displacement distributions of the first phason mode when $\alpha = 1.5$ and $k = 1$.

At last, when $\alpha = 1.5$ and $k = 1$, the stress distributions of the first phonon and phason modes for the z-FGQC half-spaces are as illustrated in Figures 8 and 9, respectively. It can be seen that the stress components T_{zz}, T_{xz}, and H_{zz} are all equal to zero at the free surface; that is, the summed traction-free boundary conditions are satisfied. Furthermore, similar to the displacement distributions in Figures 6 and 7, the penetration depth of the phason modes is also greater than that of the phonon modes. Additionally, the phonon stress components T_{zz} and T_{xz} of phonon modes are much bigger than the phason stress component H_{zz}. On the contrary, the phonon stress components T_{zz} and T_{xz} of the phason modes are much smaller than the phason stress component H_{zz}.

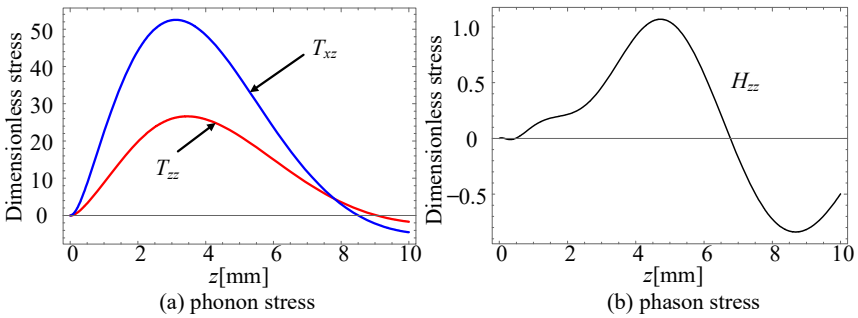

Figure 8. Stress distributions of the first phonon mode for z-FGQC halfspace when $\alpha = 1.5$ and $k = 1$.

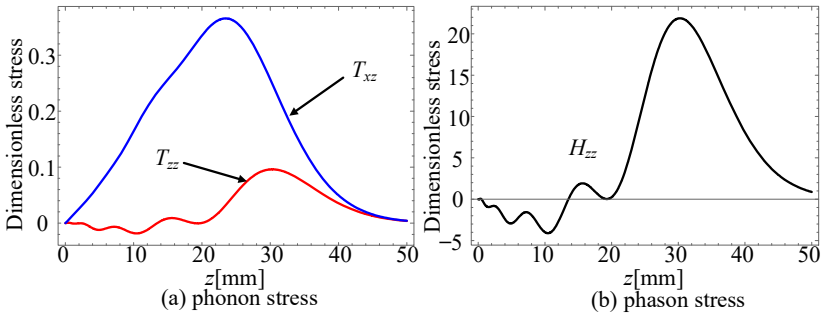

Figure 9. Stress distributions of the first phason mode for z-FGQC halfspace when $\alpha = 1.5$ and $k = 1$.

4.4. Inhomogeneity of Material

In this subsection, the influence of material inhomogeneity on wave characteristics is described. Firstly, its influence on phase velocity was analyzed. When k = 1, Figures 10 and 11 illustrate the phase velocity dispersion curves for different α values. As α increases, the phase velocities of both the phonon and phason modes decrease. The reason lies in the fact that the volume fraction of QC2 at the same depth increases with the increase in α, and the wave velocity of QC1 is higher than that of QC2. Furthermore, its influence on the first phonon mode is stronger, and the influence increases with the increase in k.

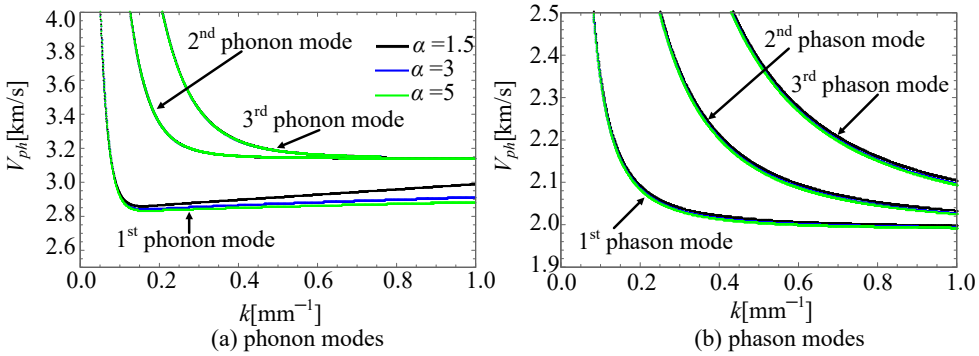

Figure 10. Phase velocity dispersion curves of z-FGQC half-spaces for different α.

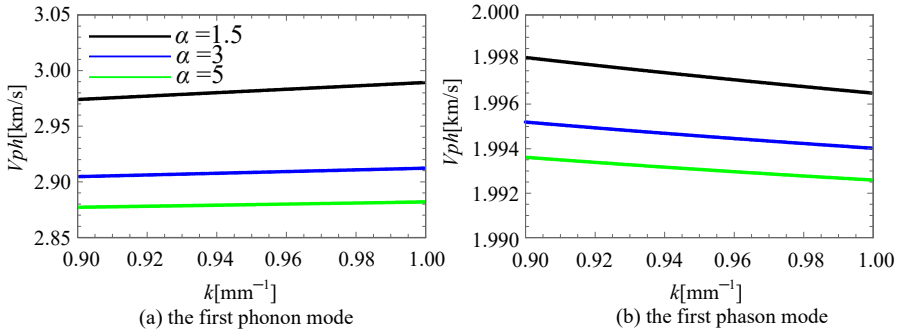

Figure 11. Partially enlarged figures from Figure 9.

Subsequently, displacement distributions of the first phonon and phason modes with different α are illustrated in Figures 12 and 13, respectively. The displacement vector of Rayleigh waves in a uniform elastic half-space is a counterclockwise ellipse at a certain depth and then gradually becomes a clockwise ellipse. The depth at which this change occurs is called the critical depth [44]. Similarly, the depth at which the phonon displacement component in the x direction changes from positive to negative is defined as the critical depth. As α increases, the critical depth decreases, and the energies are more concentrated near the top surface.

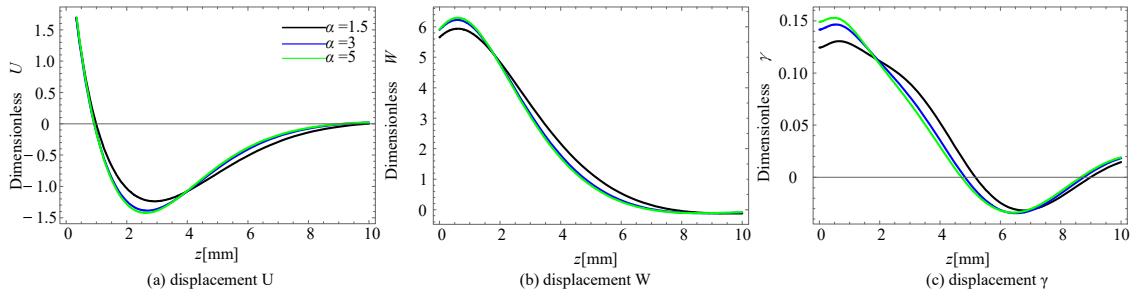

Figure 12. Displacement distributions of the first phonon mode for different α when k = 1.

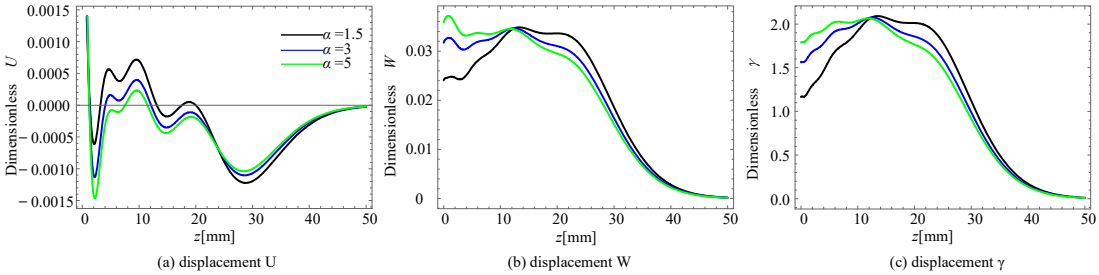

Figure 13. Displacement distributions of the first phason mode for different α when $k = 1$.

4.5. The Influence of Quasiperiodic Direction on Wave Characteristics

Firstly, the influence of the quasiperiodic direction on phase velocity was investigated. The phase velocity dispersion curves of *z*-FGQC and *x*-FGQC half-spaces are illustrated in Figure 14. Its influence on the phonon modes at low frequencies is significant but is weak on the phason modes. For the phason modes, the phase velocity of the *x*-FGQC half-space is much higher than that of the *z*-FGQC half-space. The quasiperiodic and wave propagation directions are consistent for the *x*-FGQC half-space. It can be concluded that the phase velocity is higher when the quasiperiodic and wave propagation directions are consistent.

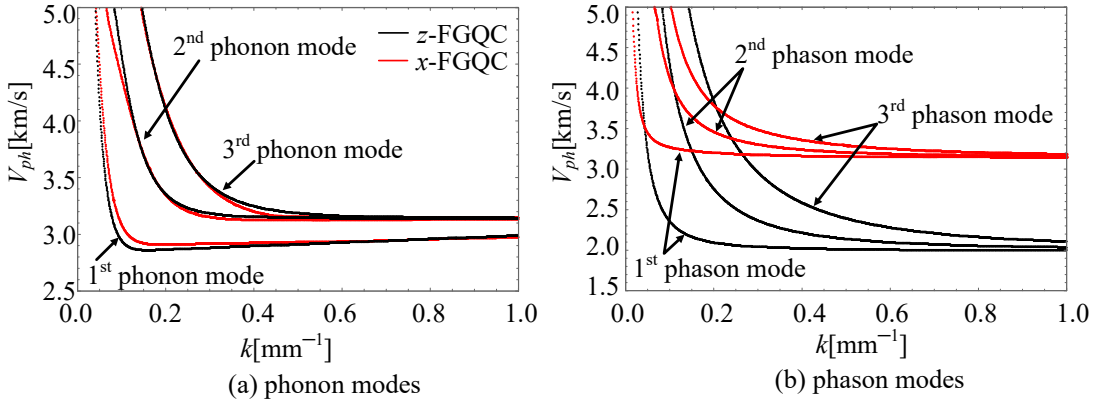

Figure 14. Phase velocity dispersion curves of *z*-FGQC and *x*-FGQC half-spaces.

Subsequently, the influence of the quasiperiodic direction on displacements was studied. When $\alpha = 1.5$ and $k = 1$, Figures 15 and 16 show the displacement distributions of the first phonon and phason modes for the *x*-FGQC half-space, respectively. Compared with Figures 6 and 7, the influence of variation in the quasiperiodic direction on phason modes is considerable. For the phonon modes, its influence on the phonon displacement components is extremely weak but is considerable on the phason displacement components.

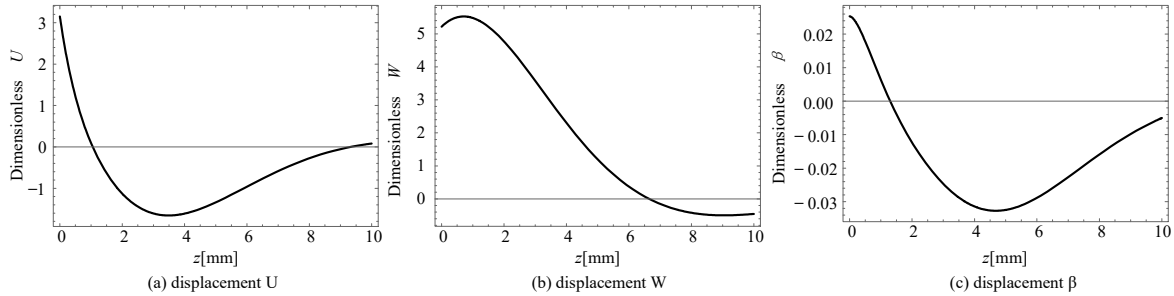

Figure 15. Displacement distributions of the first phonon mode for x-FGQC half-space when $\alpha = 1.5$ and $k = 1$.

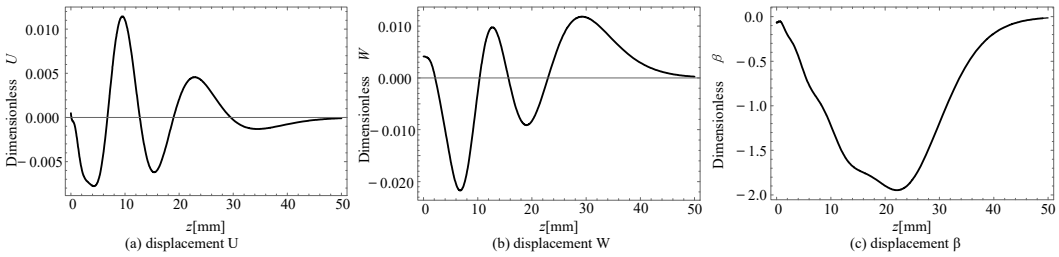

Figure 16. Displacement distributions of the first phason mode for *x*-FGQC half-space when $\alpha = 1.5$ and $k = 1$.

At last, when $\alpha = 1.5$ and $k = 1$, the stress distributions of the first phonon and phason modes for the *x*-FGQC half-spaces are as illustrated in Figures 17 and 18, respectively. It can be seen that stress components T_{zz}, T_{xz}, and H_{xz} are all equal to zero at the free surface; that is, the summed traction-free boundary conditions are satisfied.

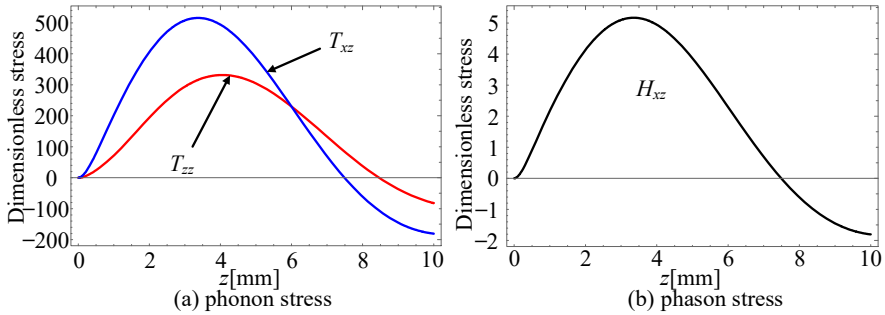

Figure 17. Stress distributions of the first phonon mode for *x*-FGQC half-space when $\alpha = 1.5$ and $k = 1$.

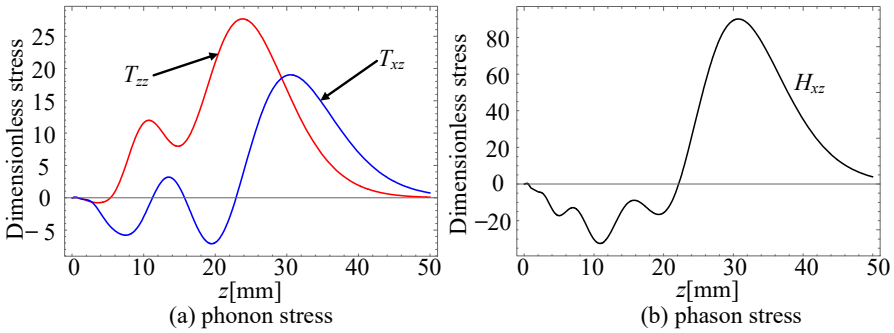

Figure 18. Stress distributions of the first phason mode for *x*-FGQC half-space when $\alpha = 1.5$ and $k = 1$.

5. Conclusions

In the present study, an analytical Laguerre orthogonal polynomials method was employed to investigate Rayleigh waves propagating in the one-dimensional hexagonal FGQC half-space. Dispersion curves and displacement and stress distributions were illustrated. The influences of the phonon–phason coupling effect, inhomogeneity, and quasi-periodic direction on wave characteristics were analyzed. According to the above numerical results, the following conclusions can be drawn:

(1) Compared with the classical Laguerre polynomial method, the improvement in computational efficiency of the analytical Laguerre polynomial method is more than 99%.
(2) The energy penetration depth of the phason modes for Rayleigh waves is greater than that of the phonon modes.
(3) The variation in the graded function has a considerable influence on the phase velocity and displacement distribution. Therefore, the performance of FGQC half-spaces can be adjustable by changing the graded function.

(4) The phase velocity of Rayleigh waves is higher when the directions of quasiperiodicity and wave propagation coincide.

Author Contributions: B.Z. and J.Y. proposed the studied problem and the corresponding solving method; H.T. conducted the theoretical derivation and the computation; B.Z., L.L. and J.D. analyzed and discussed the results; B.Z. and J.D. wrote the paper. All authors participated in the discussion and commented on the manuscript. All authors have read and agreed to the published version of the manuscript.

Funding: This research was funded by the National Natural Science Foundation of China (No. 12102131), the Innovative Research Team of Henan Polytechnic University (No. T2022-4), Henan University Science and Technology Innovation Team Support Plan (23IRTSTHN016), Research Fund for the Doctoral Program of Henan Polytechnic University (B2021-32), and Key Discipline of Mechanical Engineering in Henan Polytechnic University.

Data Availability Statement: Not applicable.

Conflicts of Interest: The authors declare no conflict of interest. The funders had no role in the study; in the writing of the manuscript; or in the decision to publish the results.

References

1. Stephens, P.W.; Goldman, A.I. Metallic Phase with Long-Range Orientational Order and No Translational Symmetry. *Phys. Rev. Lett.* **1984**, *53*, 1951–1953.
2. Hammock, D.; Fang, F.; Irwin, K. Quasicrystal Tilings in Three Dimensions and Their Empires. *Crystals* **2018**, *8*, 370. [CrossRef]
3. Li, G.; Li, L. An Analysis Method of Symplectic Dual System for Decagonal Quasicrystal Plane Elasticity and Application. *Crystals* **2022**, *12*, 636. [CrossRef]
4. Prekul, A.; Shchegolikhina, N. Two-Level Electron Excitations and Distinctive Physical Properties of Al-Cu-Fe Quasicrystals. *Crystals* **2016**, *6*, 119. [CrossRef]
5. Radi, E.; Mariano, P.M. Steady-State Propagation of Dislocations in Quasi-Crystals. *Proc. R. Soc. A* **2011**, *467*, 3490–3508. [CrossRef]
6. Sathish, S.; Kulik, A.; Gremaud, G. Elastically isotropic Al-Li-Cu quasicrystal. *Solid State Commun.* **1991**, *77*, 403–407. [CrossRef]
7. Farrokh, M.; Taheripur, M.; Carrera, E. Optimum Distribution of Materials for Functionally Graded Rectangular Plates Considering Thermal Buckling. *Compos. Struct.* **2022**, *289*, 115401. [CrossRef]
8. Zhang, R.; Jiang, F.; Xue, L.; Yu, J.Y. Review of Additive Manufacturing Techniques for Large-Scale Metal Functionally Graded Materials. *Crystals* **2022**, *12*, 858. [CrossRef]
9. Raza, A.; Talha, M.; Pathak, H. Influence of Material Uncertainty on Vibration Characteristics of Higher Order Cracked Functionally Gradient Plates Using XFEM. *INT J. Appl. Mech.* **2021**, *13*, 2150062. [CrossRef]
10. Iqbal, M.D.; Birk, C.; Ooi, E.T.; Pramod, A.L.N.; Natarajan, S.; Gravenkamp, H.; Song, C. Thermoelastic Fracture Analysis of Functionally Graded Materials Using the Scaled Boundary Finite Element Method. *Eng. Fract. Mech.* **2022**, *264*, 108305. [CrossRef]
11. Afshar, A.; Abbasi, M.; Eslami, M.R. Two-Dimensional Solution for Coupled Thermoelasticity of Functionally Graded Beams Using Semi-Analytical Finite Element Method. *Mech. Adv. Mater. Struct.* **2011**, *18*, 327–336. [CrossRef]
12. Salah, I.B.; Wali, Y.; Ghozlen, M.H.B. Love Waves in Functionally Graded Piezoelectric Materials by Stiffness Matrix Method. *Ultrasonics* **2011**, *51*, 310–316. [CrossRef]
13. Zhu, J.; Chen, W.Q.; Ye, G.R.; Fu, J.Z. Waves in fluid-filled functionally graded piezoelectric hollow cylinders: A restudy based on the reverberation-ray matrix formulation. *Wave Motion* **2013**, *50*, 415–427. [CrossRef]
14. Liu, H.; Pan, E.; Cai, Y. General Surface Loading over Layered Transversely Isotropic Pavements with Imperfect Interfaces. *Adv. Eng. Softw.* **2018**, *115*, 268–282. [CrossRef]
15. Pan, E. Green's Functions for Geophysics: A Review. *Rep. Prog. Phys.* **2019**, *82*, 106801. [CrossRef] [PubMed]
16. Cao, X.; Jin, F.; Jeon, I. Calculation of Propagation Properties of Lamb Waves in a Functionally Graded Material (FGM) Plate by Power Series Technique. *NDT E Int.* **2011**, *44*, 84–92. [CrossRef]
17. Zhang, B.; Yu, J.G.; Zhang, X.M.; Ming, P.M. Complex Guided Waves in Functionally Graded Piezoelectric Cylindrical Structures with Sectorial Cross-Section. *Appl. Math. Model.* **2018**, *63*, 288–302. [CrossRef]
18. Ferreira, T.; Koga, G.Y.; Oliveira, I.L.D.; Kiminami, C.S.; Botta, W.J.; Bolfarini, C. Functionally Graded Aluminum Reinforced with Quasicrystal Approximant Phases-Improving the Wear Resistance at High Temperatures. *Wear* **2020**, *462–463*, 203507. [CrossRef]
19. Ferreira, T.; Oliveira, I.L.D.; Zepon, G.; Bolfarini, C. Rotational Outward Solidification Casting: An Innovative Single Step Process to Produce a Functionally Graded Aluminum Reinforced with Quasicrystal Approximant Phases. *Mater. Des.* **2020**, *189*, 108544. [CrossRef]
20. Mu, X.; Xu, W.S.; Zhu, Z.W.; Zhang, L.L.; Gao, Y. Multi-field Coupling Solutions of Functionally Graded Two-Dimensional Piezoelectric Quasicrystal Wedges and Spaces. *Appl. Math. Mech.* **2022**, *109*, 251–264. [CrossRef]

21. Zhang, L.; Guo, J.H.; Xing, Y. Bending Analysis of Functionally Graded One-Dimensional Hexagonal Piezoelectric Quasicrystal Multilayered Simply Supported Nanoplates Based on Nonlocal Strain Gradient Theory. *Acta Mech. Solida Sin.* **2021**, *34*, 237–251. [CrossRef]
22. Yang, J.; Wang, X.; Ding, S.H.; Li, X. Scattering of SH Wave by a Crack in a Functionally Graded One Dimensional Hexagonal Piezoelectric Quasicrystals. *ZAMM-Z. Angew. Math. Mech.* **2023**, *103*, 202200071. [CrossRef]
23. Li, Y.; Li, Y.; Qin, Q.; Yang, L.Z.; Zhang, L.L.; Gao, Y. Axisymmetric Bending Analysis of Functionally Graded One-Dimensional Hexagonal Piezoelectric Quasi-Crystal Circular Plate. *Proc. R. Soc. A-Math. Phys.* **2020**, *476*, 2241. [CrossRef] [PubMed]
24. Zhang, B.; Yu, J.G.; Zhang, X.M. Guided Wave Propagation in Functionally Graded One-Dimensional Hexagonal Quasi-Crystal Plates. *J. Mech.* **2020**, *36*, 773–788. [CrossRef]
25. Zhang, B.; Wang, X.H.; Elmaimouni, L.; Yu, J.G.; Zhang, X.M. Axial Guided Wave Characteristics in Functionally Graded One-Dimensional Hexagonal Piezoelectric Quasi-Crystal Cylinders. *Math. Mech. Solids* **2022**, *27*, 125–143. [CrossRef]
26. Nobili, A.; Radi, E.; Signorini, C. A New Rayleigh-Like Wave in Guided Propagation of Antiplane Waves in Couple Stress Materials. *Proc. R. Soc. A* **2020**, *476*, 20190822. [CrossRef]
27. Xiang, L.; Greenshields, D.; Dixon, S.; Edwards, R.S. Phased Electromagnetic Acoustic Transducer Array for Rayleigh Wave Surface Defect Detection. *IEEE Trans. Ultrason. Ferroelectr. Freq. Control* **2020**, *67*, 1403–1411. [CrossRef]
28. Govindarajan, R.S.; Eduardo, R.N.; Kim, D. Surface Acoustic Wave-Based Flexible Piezocomposite Strain Sensor. *Crystals* **2021**, *11*, 1576. [CrossRef]
29. Maradudin, A.A.; Wallis, R.F.; Mills, D.L.; Ballard, R.L. Vibrational Edge Modes in Finite Crystals. *Phys. Rev. B* **1972**, *6*, 1106–1111. [CrossRef]
30. Li, K.; Jing, S.; Yu, J.G.; Zhang, X.M.; Zhang, B. The Complex Rayleigh Waves in a Functionally Graded Piezoelectric Half-Space: An Improvement of the Laguerre Polynomial Approach. *Materials* **2020**, *13*, 2320. [CrossRef]
31. Matar, O.B.; Gasmi, N.; Zhou, H.; Goueygou, M.; Talbi, A. Legendre and Laguerre Polynomial Approach for Modeling of Wave Propagation in Layered Magneto-Electro-Elastic Media. *J. Acoust. Soc. Am.* **2013**, *133*, 1415–1424. [CrossRef] [PubMed]
32. Maradudin, A.A.; Subbaswamy, K.R. Edge Localized Vibration Modes on a Rectangular Ridge. *JAP* **1977**, *48*, 3410–3414. [CrossRef]
33. Zhang, B.; Yu, J.G.; Zhang, X.M. Love Waves in Multilayered Elastic Half-Space: An Improved Orthogonal Polynomials Method. In Proceedings of the 2015 Symposium on Piezoelectricity, Acoustic Waves and Device Applications, Jinan, China, 30 October–2 November 2015; pp. 269–272.
34. Yu, J.G.; Wang, X.H.; Zhang, X.M. An Analytical Integration Legendre Polynomial Series Approach for Lamb Waves in Fractional Order Thermoelastic Multilayered Plates. *Math. Method Appl. Sci.* **2022**, *45*, 7631–7651. [CrossRef]
35. Waksmanski, N.; Pan, E.; Yang, L.Z.; Gao, Y. Harmonic Response of Multilayered One-Dimensional Quasicrystal Plates Subjected to Patch Loading. *J. Sound Vib.* **2016**, *375*, 237–253. [CrossRef]
36. Hosseini, S.M.; Sladek, J.; Sladek, V. Elastodynamic Analysis of a Hollow Cylinder with Decagonal Quasicrystal Properties: Meshless Implementation of Local Integral Equations. *Crystals* **2016**, *6*, 94. [CrossRef]
37. Lefebvre, J.E.; Yu, J.G.; Ratolojanahary, F.E.; Elmaimouni, L.; Xu, W.J.; Gryba, T. Mapped Orthogonal Functions Method Applied to Acoustic Waves-Based Devices. *AIP Adv.* **2016**, *6*, 065307. [CrossRef]
38. Yu, J.; Guo, J. Analytical Solution for a 1D Hexagonal Quasicrystal Strip with Two Collinear Mode-III Cracks Perpendicular to the Strip Boundaries. *Crystals* **2023**, *13*, 661. [CrossRef]
39. Liu, C.C.; Yu, J.G.; Zhang, B.; Zhang, X.M.; Wang, X.H.; Elmaimouni, L. Size-Dependent and Piezoelectric Effects on SH Wave Propagation in Functionally Graded Plates. *Mech. Res. Commun.* **2022**, *124*, 103965. [CrossRef]
40. Wang, X.H.; Li, F.L.; Zhang, B.; Yu, J.G.; Zhang, X.M. Wave Propagation in Thermoelastic Inhomogeneous Hollow Cylinders by Analytical Integration Orthogonal Polynomial Approach. *Appl. Math. Model.* **2021**, *99*, 57–80. [CrossRef]
41. Graham, R.L.; Knuth, D.E.; Patashnik, O. *Concrete Mathematics: A Foundation for Computer Science*, 2nd ed.; Addison-Wesley: Reading, MA, USA, 1994.
42. Vrettos, C. The Boussinesq Problem for Soils with Bounded Non-Homogeneity. *Int. J. Numer. Anal. Met.* **1998**, *22*, 655–669. [CrossRef]
43. Rose, J.L. *Ultrasonic Waves in Solid Media*; Cambridge University Press: Cambridge, UK, 1999.
44. Chai, H.Y. *Surface Wave Theory in Elastic Media and Its Application in Geotechnical Engineering*; Science Press: Beijing, China, 2008.

Disclaimer/Publisher's Note: The statements, opinions and data contained in all publications are solely those of the individual author(s) and contributor(s) and not of MDPI and/or the editor(s). MDPI and/or the editor(s) disclaim responsibility for any injury to people or property resulting from any ideas, methods, instructions or products referred to in the content.